AMERICAN SOCIETY FOR MICROBIOLOGY | Molecular and Cellular Biology®

RESEARCH ARTICLE

FBXL5 Inactivation in Mouse Brain Induces Aberrant Proliferation of Neural Stem Progenitor Cells

Takayoshi Yamauchi, Masaaki Nishiyama, Toshiro Moroishi, Atsuki Kawamura, Keiichi I. Nakayama

Department of Molecular and Cellular Biology, Medical Institute of Bioregulation, Kyushu University, Fukuoka, Japan

ABSTRACT FBXL5 is the substrate recognition subunit of an SCF-type ubiquitin ligase that serves as a master regulator of iron metabolism in mammalian cells. We previously showed that mice with systemic deficiency of FBXL5 fail to sense intracellular iron levels and die *in utero* at embryonic day 8.5 (E8.5) as a result of iron overload and subsequent oxidative stress. This early embryonic mortality has thus impeded study of the role of FBXL5 in brain development. We have now generated mice lacking FBXL5 specifically in nestin-expressing neural stem progenitor cells (NSPCs) in the brain. Unexpectedly, the mutant embryos manifested a progressive increase in the number of NSPCs and astroglia in the cerebral cortex. Stabilization of iron regulatory protein 2 (IRP2) as a result of FBXL5 deficiency led to accumulation of ferrous and ferric iron as well as to generation of reactive oxygen species. Pharmacological manipulation suggested that the phenotypes of FBXL5 deficiency are attributable to aberrant activation of mammalian target of rapamycin (mTOR) signaling. Our results thus show that FBXL5 contributes to regulation of NSPC proliferation during mammalian brain development.

KEYWORDS SCF complex, brain development, iron regulation, ligase, mTOR, neural stem cell, oxidative stress, ubiquitination

Received 19 August 2016 **Returned for modification** 13 September 2016 **Accepted** 3 January 2017

Accepted manuscript posted online 9 January 2017

Citation Yamauchi T, Nishiyama M, Moroishi T, Kawamura A, Nakayama KI. 2017. FBXL5 inactivation in mouse brain induces aberrant proliferation of neural stem progenitor cells. Mol Cell Biol 37:e00470-16. https://doi.org/10.1128/MCB.00470-16.

Address correspondence to Masaaki Nishiyama, nishiyam@bioreg.kyushu-u.ac.jp, or Keiichi I. Nakayama, nakayak1@bioreg.kyushu-u.ac.jp.

Iron is an essential element for fundamental biological processes such as oxygen transport, DNA synthesis, and oxidative phosphorylation (1). When iron is present in excess, however, its ability to readily gain and lose electrons results in the formation of damaging hydroxyl and lipid radicals (2). Iron levels are therefore strictly regulated at both cellular and systemic levels, with aging and numerous pathological conditions, including metabolic disorders, anemia, infections, and cancer, being associated with iron dysregulation (3–5).

FBXL5 (F box and leucine-rich repeat protein 5) is a member of the F-box family of proteins, which function as substrate recognition adapters for SCF-type ubiquitin ligases (6, 7). FBXL5 senses iron and oxygen through its NH_2-terminal hemerythrin-like domain and promotes the degradation of iron regulatory protein 1 (IRP1) and IRP2 (8, 9), with regulation by the FBXL5-IRP axis being essential for the maintenance of iron homeostasis at the cellular and systemic levels (10). IRPs are cytosolic RNA-binding proteins and bind certain mRNAs that contain iron-responsive elements (IREs) and encode proteins required for iron homeostasis, with such binding regulating the translation or stability of these mRNAs (2). Under iron-limiting conditions, IRPs are stabilized and participate in inhibitory binding to IREs in the 5′ untranslated region (UTR) of mRNAs for ferritin (which mediates iron storage) and ferroportin (which mediates iron export), whereas their binding to IREs in the 3′ UTR of mRNAs for transferrin receptor 1 (TfR1, which mediates iron uptake) and divalent metal transporter 1 (DMT1, which mediates iron transport) suppresses mRNA degradation by nucleases

and thereby promotes synthesis of the encoded proteins. Together, these effects lead to an increase in the size of the labile iron pool. FBXL5 deficiency results in sustained accumulation of IRPs and unregulated iron uptake, eventually leading to iron overload and the generation of reactive oxygen species (ROS) (10, 11).

The precise regulation of cell cycle progression and cell growth is essential for development of the nervous system (12, 13). Neuroepithelial cells in the apical region of the developing mammalian neocortex give rise to neural stem progenitor cells (NSPCs), postmitotic neurons, and glial cells in a temporally and spatially controlled manner. Although several signaling pathways, including those mediated by Wnt, Sonic hedgehog, Notch, and fibroblast growth factor (FGF)–phosphatidylinositol 3-kinase (PI3K), have been shown to regulate the proliferation and development of NSPCs (12, 14), the manner in which such signaling is maintained by metabolic conditions to achieve proper control of neurogenesis remains a central question in neurodevelopmental biology (15, 16).

Recent studies suggest that iron metabolism plays an integral role in the maintenance of brain homeostasis, with abnormal accumulation of iron in the brain having been found to underlie the pathogenesis of several neurodegenerative diseases as well as neuropsychiatric disorders at various developmental stages (17–19). Iron deposits have thus been found in the substantia nigra and globus pallidus of individuals with such conditions, whereas other brain regions such as the cortex and hippocampus amass both ferric and ferrous iron (20–22). Changes in NSPC proliferation, differentiation, and survival, as well as in neurite outgrowth and dendritic spine formation induced by excess iron, have been linked to various aspects of disease pathogenesis, but the metabolic and molecular consequences of iron excess remain largely unknown (23, 24). A better understanding of how NSPCs are influenced by changes in iron availability would thus be expected to provide insights into the complex nature of NSPC biology in both normal and diseased states.

To examine how iron regulation contributes to neuronal development and maintenance, we generated mice that lack FBXL5 specifically in embryonic NSPCs. We found that such FBXL5 ablation resulted in unregulated proliferation of NSPCs and consequent defects in neurogenesis in the embryonic brain. The proliferative and functional changes in NSPCs were associated with oxidative stress and activation of PI3K-Akt-mTOR (mammalian target of rapamycin) signaling. Our results reveal the importance of the regulation of iron metabolism in NSPCs and may have implications for a variety of brain diseases.

RESULTS

Targeted inactivation of *Fbxl5* in NSPCs promotes cell proliferation. To explore the importance of homeostatic iron regulation in NSPCs, we crossed previously established *Fbxl5* floxed (*Fbxl5*$^{flox/flox}$) mice (10) with mice harboring a *Cre* transgene under the control of the *Nestin* promoter (*Nestin-Cre* mice) and thereby obtained *Nestin-Cre/Fbxl5*$^{flox/flox}$ mice (here referred to as *Fbxl5* conditional knockout [cKO] mice). Cre recombinase-mediated deletion of *Fbxl5* reduced the abundance of the corresponding mRNA in the embryonic brain to ~35% of that in *Fbxl5*$^{flox/flox}$ (control) mice (Fig. 1A and B). This reduced abundance of *Fbxl5* mRNA was associated with an increased amount of IRP2 protein, which in turn was accompanied by increased expression of TfR1 and decreased expression of ferritin in the forebrain of *Fbxl5* cKO mice (Fig. 1C). Similar changes in protein abundance were not apparent in the liver of *Fbxl5* cKO mice (Fig. 1C), suggesting that deletion of *Fbxl5* was specific to the central nervous system. Newborn mutant mice died within a day of delivery and were readily distinguished from control animals by their overall appearance, characterized by a curled posture (kyphosis) and drooping forelimbs (Fig. 1D and E), both features which are often observed in newborn mice with a neuromotor defect (25). Given that pulmonary alveoli were not inflated in the mutant offspring (Fig. 1F), apnea is likely responsible for the neonatal lethality.

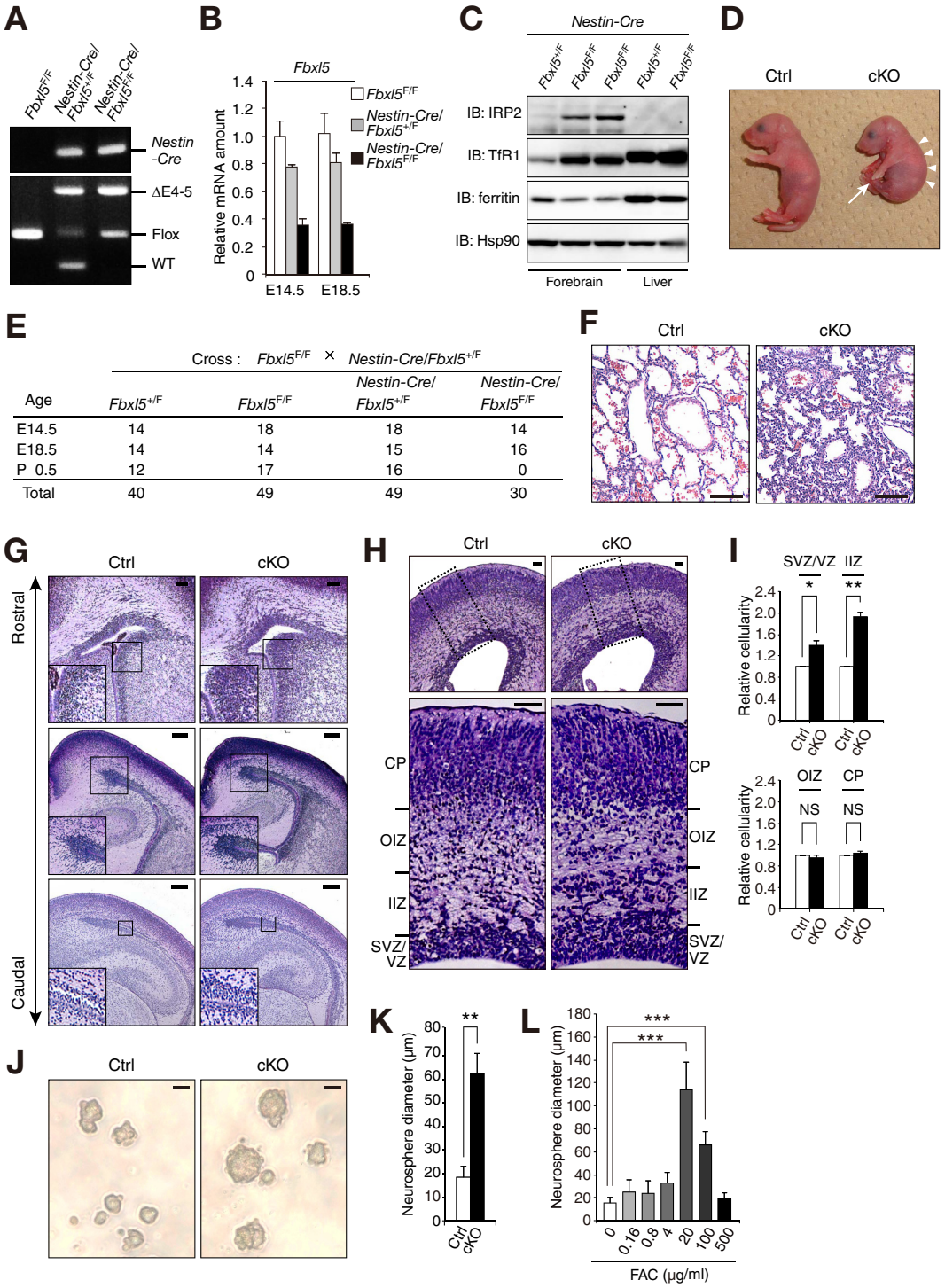

FIG 1 Targeted deletion of *Fbxl5* in embryonic NSPCs impairs brain development and induces neonatal death. (A) PCR analysis of genomic DNA isolated from the forebrain of mice of the indicated genotypes at E18.5. The positions of amplified fragments corresponding to wild-type (WT), floxed (Flox), and deleted (exons 4 and 5, ΔE4–5) alleles of *Fbxl5* as well as to the *Nestin-Cre* transgene are indicated. $Fbxl5^{F/F}$, $Fbxl5^{flox/flox}$; $Fbxl5^{+/F}$, $Fbxl5^{+/flox}$. (B) RT and real-time PCR analysis of *Fbxl5* mRNA in the forebrain of mice of the indicated genotypes at E14.5 and E18.5. Normalized data are expressed relative to the value for $Fbxl5^{flox/flox}$ mice at E14.5 and are from three independent experiments. (C) Lysates of the forebrain or liver from mice of the indicated genotypes at postnatal day 0.5 were subjected to immunoblot (IB) analysis with antibodies to the indicated proteins. Hsp90 was examined as a loading control. (D) Overall appearance of control (Ctrl) and *Nestin-Cre/*$Fbxl5^{flox/flox}$ (*Fbxl5* cKO) mice at postnatal day 0.5. The mutant embryo manifests drooping forelimbs (arrow) and abnormal body curvature (arrowheads). (E) Summary of genotypes determined for live embryos generated from intercrosses of $Fbxl5^{flox/flox}$ males with *Nestin-Cre/*$Fbxl5^{+/flox}$ females or of *Nestin-Cre/*$Fbxl5^{+/flox}$ males with $Fbxl5^{flox/flox}$

(Continued on next page)

To examine whether *Fbxl5* cKO mice manifest abnormal brain development, we subjected brain sections from embryos or neonates to histological analysis. *Fbxl5* cKO mice showed increased cell numbers in several brain regions (Fig. 1G). Specifically, whereas the number of cells in the cortical plate (CP) or outer intermediate zone (IZ) of the cortex did not differ significantly between *Fbxl5* cKO and control mice at embryonic day 18.5 (E18.5), the numbers of immature cells in the cortical ventricular/subventricular zone (VZ/SVZ) and the inner IZ were increased by ~40% and ~90%, respectively, in the mutant (Fig. 1H and I). Consistent with these results, cultured neurospheres derived from the mutant embryos were larger than those from control littermates (Fig. 1J and K). The addition of moderate amounts of ferric iron to the culture medium resulted in a marked increase in the diameter of neurospheres from control embryos (Fig. 1L), indicating that iron promotes the proliferation of VZ/SVZ-derived cells.

We hypothesized that loss of FBXL5 might affect the proliferation or survival of NSPCs, with such an effect accounting for the increased cell numbers in the VZ/SVZ and inner IZ of the *Fbxl5* cKO brain. Whereas the frequencies of apoptotic cells in the VZ/SVZ and IZ regions of the cortex did not differ significantly between the two *Fbxl5* genotypes, it was markedly increased in the CP of the *Fbxl5* cKO brain at E18.5 (Fig. 2A and B). The number of proliferating cells marked with antibodies to phosphorylated histone H3 (pHH3) was increased in the VZ/SVZ of the frontal cortex of the cKO mice compared with the level in control mice (Fig. 2C and D). The number of cells positive for the mitotic marker Ki67 was also increased in both the VZ/SVZ of the cortex and the lateral ganglionic eminence of the mutant (Fig. 2E to H). Consistent with these results, the number of cells positive for both bromodeoxyuridine (BrdU) incorporation and Ki67 in the VZ/SVZ of the cortex was increased by ~30% in the mutant (Fig. 2I and J), whereas the frequency of cells that had recently exited from the cell cycle ($BrdU^+$/$Ki67^-$) was significantly lower in the mutant mice than in control animals (Fig. 2K and L), indicating that more cells were engaged in cell division in the brain of *Fbxl5* cKO embryos than in the control brain. Together, these results suggested that more cells are produced in the VZ/SVZ but that more cells die at the CP in the mutant brain than in the control brain, with the overall size of the brain of cKO embryos thus remaining unchanged.

FBXL5 ablation alters NSPC function. Recent models suggest that a reduced level of cell cycle exit and generation of basally located intermediate progenitors would affect corticogenesis (26–28). To explore potential NSPC abnormalities in *Fbxl5* cKO mice, we evaluated brain cell composition with the use of various cell lineage markers. Whereas the frequencies of Pax6-positive radial glial cells and nestin-positive stem and progenitor cells in the cortex did not differ significantly between *Fbxl5* cKO and control mice at E14.5 (Fig. 3A, B, and I), the number of nestin-positive cells was substantially greater in the mutant, in particular, in the VZ/SVZ, at E18.5 (Fig. 3C and I). The number of Tbr2-positive intermediate progenitor cells was also increased in the mutant at E18.5 (Fig. 3D and I). We next examined whether the additional NSPCs generated in *Fbxl5* cKO mice contribute to formation of the specific layers of the CP. We detected an increase

FIG 1 Legend (Continued)
females. All genotypes at E14.5, E18.5, and postnatal day 0.5 (P0.5) are expected in equal numbers. (F) H&E staining of lung tissue from control and *Fbxl5* cKO mice at postnatal day 0.5. Scale bars, 100 μm. (G) H&E staining of the cerebrum from control and cKO mice at postnatal day 0.5. The rostral-caudal axis for the sections is indicated, and the boxed areas are shown at higher magnification in the insets. Scale bars, 200 μm. (H) H&E staining of coronal sections of the forebrain of control and cKO mice at E18.5. The boxed regions in the upper panels are shown at higher magnification in the lower panels. CP, cortical plate; OIZ, outer intermediate zone; IIZ, inner intermediate zone; SVZ, subventricular zone; VZ, ventricular zone. Scale bars, 50 μm. (I) Relative cell numbers in the VZ/SVZ, IIZ, OIZ, and CP for each genotype ($n = 3$ mice, >6 sections per mouse) determined from sections similar to those in shown in panel H. (J) Representative phase-contrast images of primary cultured neurospheres derived from control and *Fbxl5* cKO mice at E14.5. Scale bar, 50 μm. (K) Neurosphere diameter determined in three independent experiments for cultures similar to those shown in panel J maintained for 3 days. (L) Neurosphere diameter determined in three independent experiments for cultures derived from control embryos and maintained for 3 days in the presence of the indicated concentrations of ferric ammonium citrate (FAC). Sections from control and *Fbxl5* cKO mice were processed in parallel and imaged at the same settings. All quantitative data are means ± SEM. *, $P < 0.05$; **, $P < 0.01$; ***, $P < 0.001$ (Student's *t* test). NS, not significant.

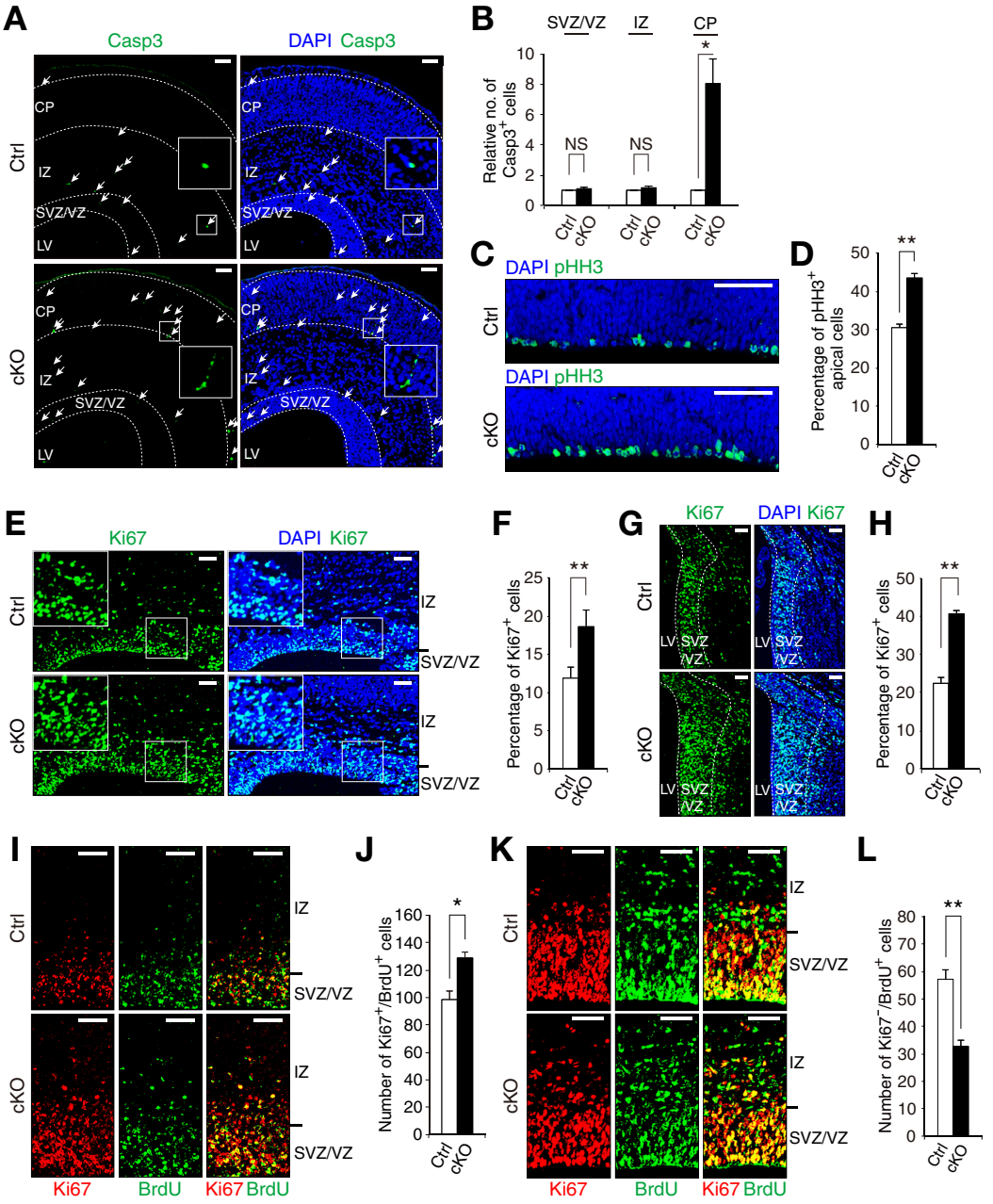

FIG 2 Ablation of FBXL5 results in increased proliferation of NSPCs. (A) Immunohistofluorescence analysis of cleaved caspase-3 (Casp3) in representative sections of the cerebral cortex of control and *Fbxl5* cKO mice at E18.5. Nuclei were counterstained with DAPI. The boxed areas are shown at higher magnification in the insets. Arrows mark apoptotic cells. LV, lateral ventricle. (B) Quantification of Casp3-positive cells in the indicated regions of the control and *Fbxl5* cKO cortex ($n = 3$ mice, three sections per mouse) determined from sections similar to those shown in panel A. (C) Immunohistofluorescence staining of phosphorylated histone H3 (pHH3) in coronal sections of the cortex of each genotype at E16.5. Nuclei were stained with DAPI. (D) Quantification of pHH3$^+$ apical cells in sections ($n = 3$ mice, three sections per mouse) similar to those shown in panel C. (E) Immunohistofluorescence staining of Ki67 in coronal sections of the control and *Fbxl5* cKO cortex at E18.5. Nuclei were stained with DAPI. The boxed areas are shown at higher magnification in the insets. (F) Quantification of Ki67$^+$ cells in the VZ/SVZ ($n = 3$ mice, three sections per mouse) determined from sections similar to those shown in panel E. (G) Immunohistofluorescence analysis of Ki67 in coronal sections of the lateral ganglionic eminence of each genotype at E18.5. Nuclei were stained with DAPI. (H) Quantification of Ki67$^+$ cells in sections ($n = 3$ mice, three sections per mouse) similar to those shown in panel G. (I) Immunohistofluorescence staining of Ki67 and BrdU in the cortex of each genotype at 1 h after pulse-labeling with BrdU in E18.5 embryos. (J) Quantification of the number of cells positive for both Ki67 and BrdU determined from sections ($n = 3$ mice, three sections per mouse) similar to those shown in panel I. (K) Immunohistofluorescence analysis of Ki67 and BrdU in the cortex of each genotype at 24 h after pulse-labeling with BrdU in E14.5 embryos. (L) Quantification of the number of cells negative for Ki67 but positive for BrdU determined from sections ($n = 3$ mice, three sections per mouse) similar to those shown in panel K. Sections from control and *Fbxl5* cKO mice were processed in parallel and imaged at the same settings. Scale bars, 50 μm. All quantitative data are means ± SEM. *, $P < 0.05$; **, $P < 0.01$ (Student's *t* test).

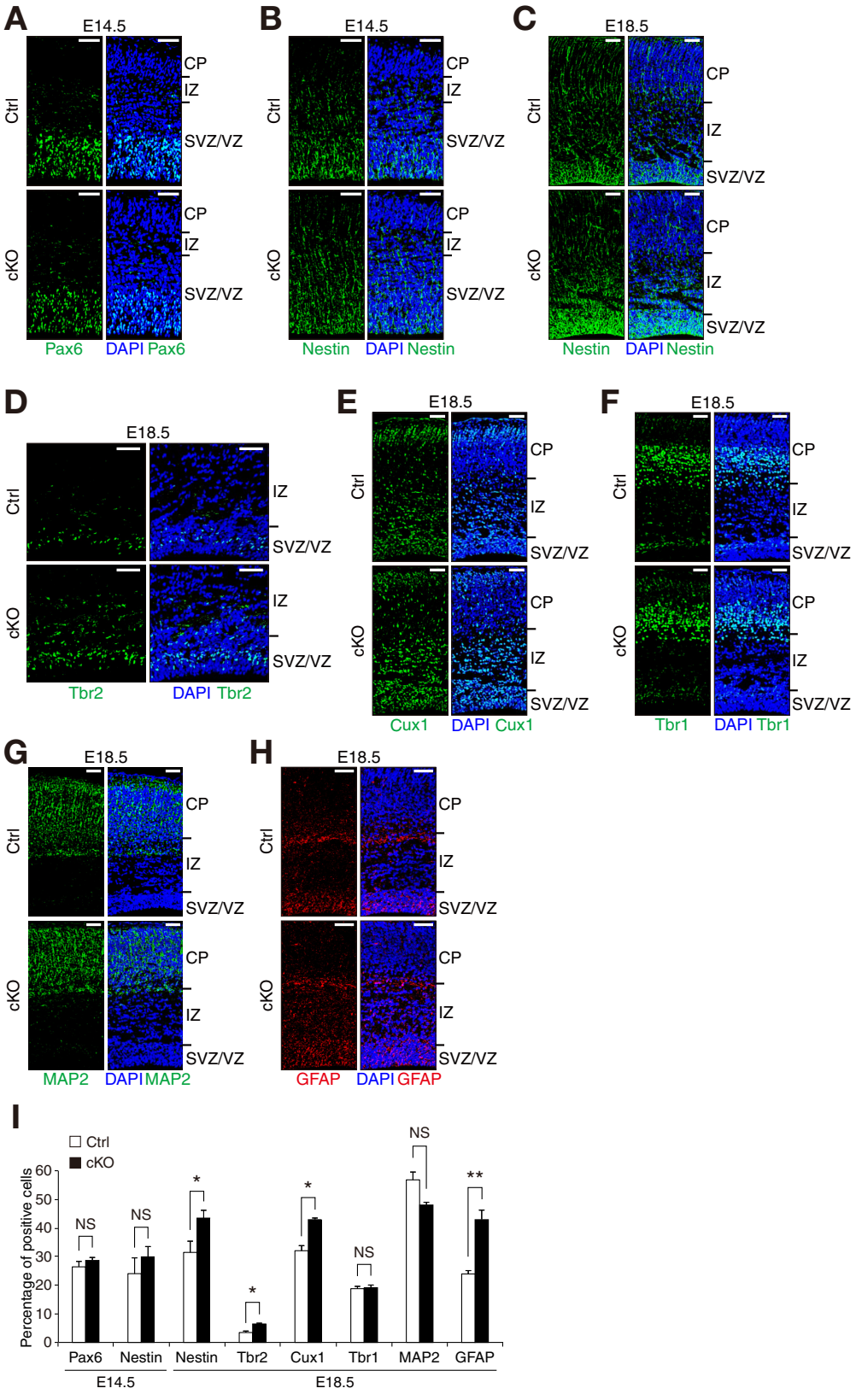

FIG 3 FBXL5 ablation alters NSPC differentiation in the brain. (A and B) Immunohistofluorescence staining of Pax6 or nestin in coronal sections of the cortex of control and *Fbxl5* cKO mice at E14.5. Nuclei were stained with DAPI. Scale bars, 50 μm. (C to H) Immunohistofluorescence staining of nestin, Tbr2, Cux1, Tbr1, MAP2, or GFAP, as indicated, in coronal sections of the cortex at E18.5. Nuclei were stained with DAPI. Scale bars, 50 μm. (I) Quantification of immunoreactive cells in the cortex of each genotype ($n = 3$ mice, >6 sections per mouse) determined from sections similar to those shown in panels A to H. Data are means ± SEM. *, $P < 0.05$; **, $P < 0.01$ (Student's *t* test).

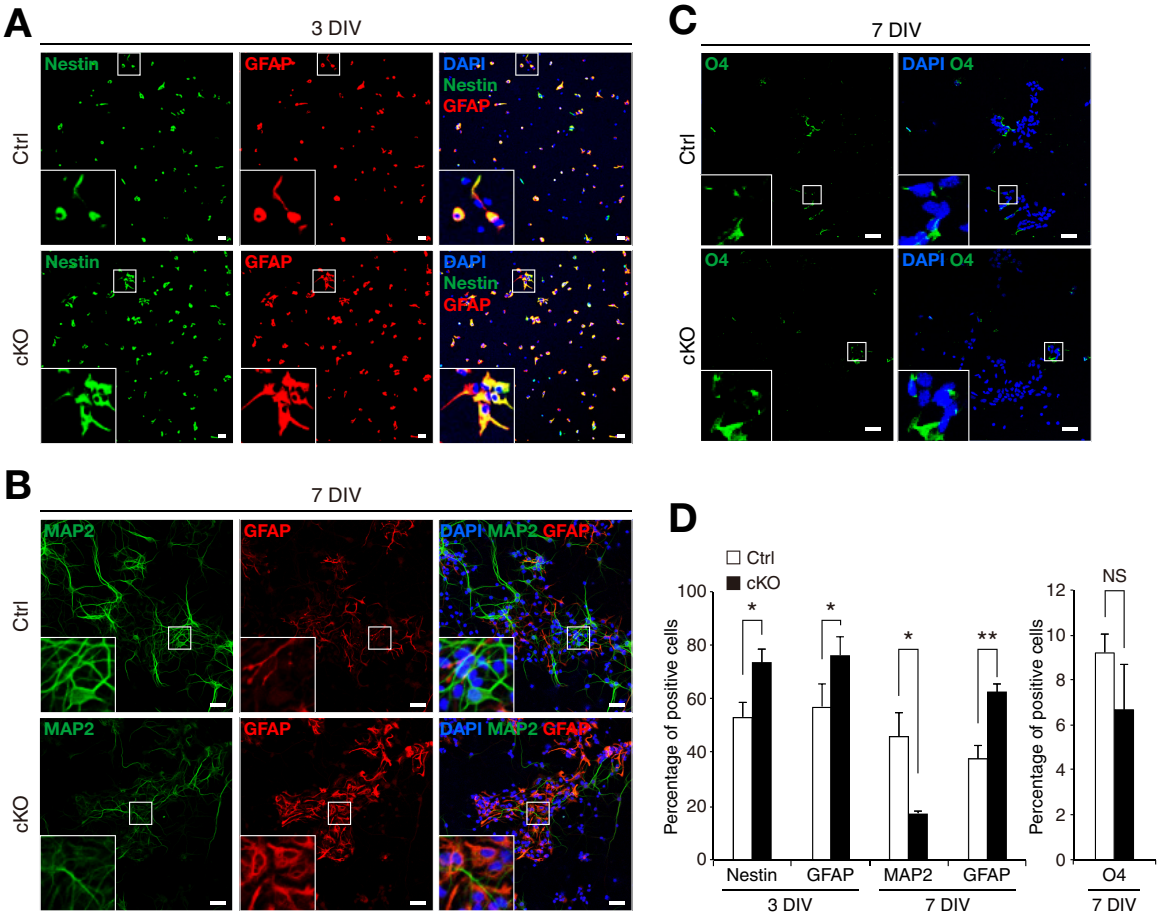

FIG 4 FBXL5 deficiency results in retention of immature cells and promotes astrogliogenesis *in vitro*. (A to C) Immunocytofluorescence analysis of nestin and GFAP, MAP2 and GFAP, or O4, as indicated, in neurosphere cultures derived from control or *Fbxl5* cKO embryos and induced to differentiate for the indicated times. The boxed areas are shown at higher magnification in the insets. Nuclei were stained with DAPI. Scale bars, 50 μm. (D) Quantification of nestin-, GFAP-, MAP2-, or O4-positive cells at 3 or 7 days *in vitro* (DIV) for cultures similar to those in shown in panels A to C. Data are means ± SEM from three independent experiments. *, $P < 0.05$; **, $P < 0.01$ (Student's *t* test).

in the total number of Cux1-positive neuronal cells although such an increase was not apparent in the cohesive outer layers (layers II to IV) of the mutant brain sections (Fig. 3E and I). The number of cells expressing other neuronal markers, such as Tbr1 (layer VI) and microtubule-associated protein 2 (MAP2), was either unaffected or tended to be reduced in the mutant cortex (Fig. 3F, G, and I). These results thus suggested that fewer upper-layer neurons were produced in the E18.5 *Fbxl5* cKO brain, whereas the number of neurons in lower layers was not affected. In contrast, the number of glial fibrillary acidic protein (GFAP)-positive astrocytes in the IZ was substantially increased in the mutant cortex (Fig. 3H and I).

To recapitulate the effects of FBXL5 inactivation on NSPC differentiation in an *in vitro* system, we induced the differentiation of control and mutant neurospheres by withdrawing growth factors from the culture medium and adding fetal bovine serum for 3 to 7 days (Fig. 4). The frequencies of nestin-positive and GFAP-positive cells were increased for the mutant neurospheres compared with levels in the control cultures after 3 days of differentiation (Fig. 4A and D). At 7 days *in vitro*, the percentage of GFAP-positive astrocytes was markedly increased for the *Fbxl5* cKO cells compared with the level in the control cells (Fig. 4B and D), whereas that of MAP2-positive neurons was reduced (Fig. 4B and D) and that of O4-positive oligodendrocytes was unchanged (Fig. 4C and D). These results thus suggested that differentiation of the mutant NSPCs in culture was skewed toward astrocytes, consistent with our *in vivo* findings (Fig. 3I).

Iron accumulation induces oxidative stress in the *Fbxl5* cKO brain. Given that both accumulation of IRPs and iron deposition were previously observed in *Fbxl5*$^{-/-}$ embryos (10), we examined the brain of *Fbxl5* cKO embryos for similar effects. As in *Fbxl5*$^{-/-}$ embryos, we found that the abundance of TfR1 mRNA was markedly increased in the brain of *Fbxl5* cKO embryos compared with the level in control embryos (Fig. 5A). Immunoblot analysis also revealed accumulation of IRP2 (but not that of IRP1) in the forebrain of *Fbxl5* cKO embryos, which likely accounted for the associated upregulation of TfR1 (Fig. 5B). We next investigated the effects of such IRP2 upregulation on cellular iron homeostasis. We thus examined the abundance of iron in serial brain sections of E18.5 embryos with the use of diaminobenzidine (DAB)-enhanced Turnbull and Perls' stains, which are specific for ferrous (Fe^{2+}) and ferric (Fe^{3+}) iron, respectively (29). Both ferrous and ferric iron deposition was detected in the mutant cortex (Fig. 5C). The nonheme iron content of the brain, but not that of the liver, was also increased in *Fbxl5* cKO embryos (Fig. 5D).

The increased iron abundance in the mutant brain would be expected to induce ROS production, given that intracellular free iron induces oxidative stress (30). Consistent with this notion, the fluorescence emitted by the ROS-sensitive dye 2′,7′-dichlorofluorescein diacetate (DCFDA) was significantly increased in neurospheres derived from *Fbxl5* cKO embryos compared with that from control embryos (Fig. 5E). In addition, the expression levels of genes for catalase, glutathione peroxidase 1 (GPx1), and superoxide dismutase 1 (SOD1), which is upregulated by ROS, were found to be significantly increased in the forebrain of mutant embryos (Fig. 5F). Importantly, exposure of mutant neurospheres to the antioxidant *N*-acetylcysteine (NAC) for 3 days under differentiation-inducing conditions was sufficient to reduce the number of nestin-immunoreactive cells to control levels (Fig. 5G and H). These results thus suggested that FBXL5 is required for proper control of the abundance of proteins that contribute to iron homeostasis and consequent prevention of oxidative stress during corticogenesis.

The mTOR pathway is activated in the *Fbxl5* cKO brain. ROS have been shown to activate the PI3K-Akt-mTOR pathway through reversible inactivation of phosphatase and tensin homolog (PTEN) in NSPCs (31–33). Consistent with this finding, immunoblot analysis revealed that the fraction of oxidized PTEN was increased in the forebrain of *Fbxl5* cKO mice at E18.5 (Fig. 6A). Evaluation of the activation status of key downstream molecules in the PI3K-Akt-mTOR pathway revealed that the phosphorylation levels of Akt, ribosomal protein S6, and 4E-BP1 in the forebrain were increased in the mutant compared with levels in the control (Fig. 6B). Of note, the phosphorylation of signal transducer and activator of transcription 3 (STAT3) was markedly increased in the mutant, consistent with the previous observation that STAT3 phosphorylation was increased in mice that lack tuberous sclerosis complex (TSC) and show hyperactivation of mTOR (34). The levels of the mTOR-associated proteins Raptor and Rictor did not differ between *Fbxl5* cKO and control mice (Fig. 6B). Immunohistofluorescence analysis also showed an increased level of S6 phosphorylation in the cortex of the mutant animals at E18.5 (Fig. 6C and D). Furthermore, the stimulatory effect of elevated ROS levels in FBXL5-deficient NSPCs on the number of nestin-positive cells in differentiating neurospheres was abolished by the PI3K inhibitor LY294002 (Fig. 6E and F), suggesting that this effect may be dependent on the PI3K pathway.

To examine whether the aberrant proliferation and differentiation of NSPCs in *Fbxl5* cKO mice are indeed attributable to mTOR activation, we examined whether pharmacological inhibition of mTOR might reverse *Fbxl5* mutant phenotypes. Treatment of pregnant dams with rapamycin at E14.5 attenuated the difference in cellularity of the VZ/SVZ and inner IZ regions apparent between *Fbxl5* cKO and control embryos at E18.5 (Fig. 7A and B). In addition, the increase in the number of NSPCs positive for nestin and Ki67 was no longer apparent in mutant embryos exposed to rapamycin (Fig. 7C and D). Immunoblot analysis also revealed that the increase in the phosphorylation level of

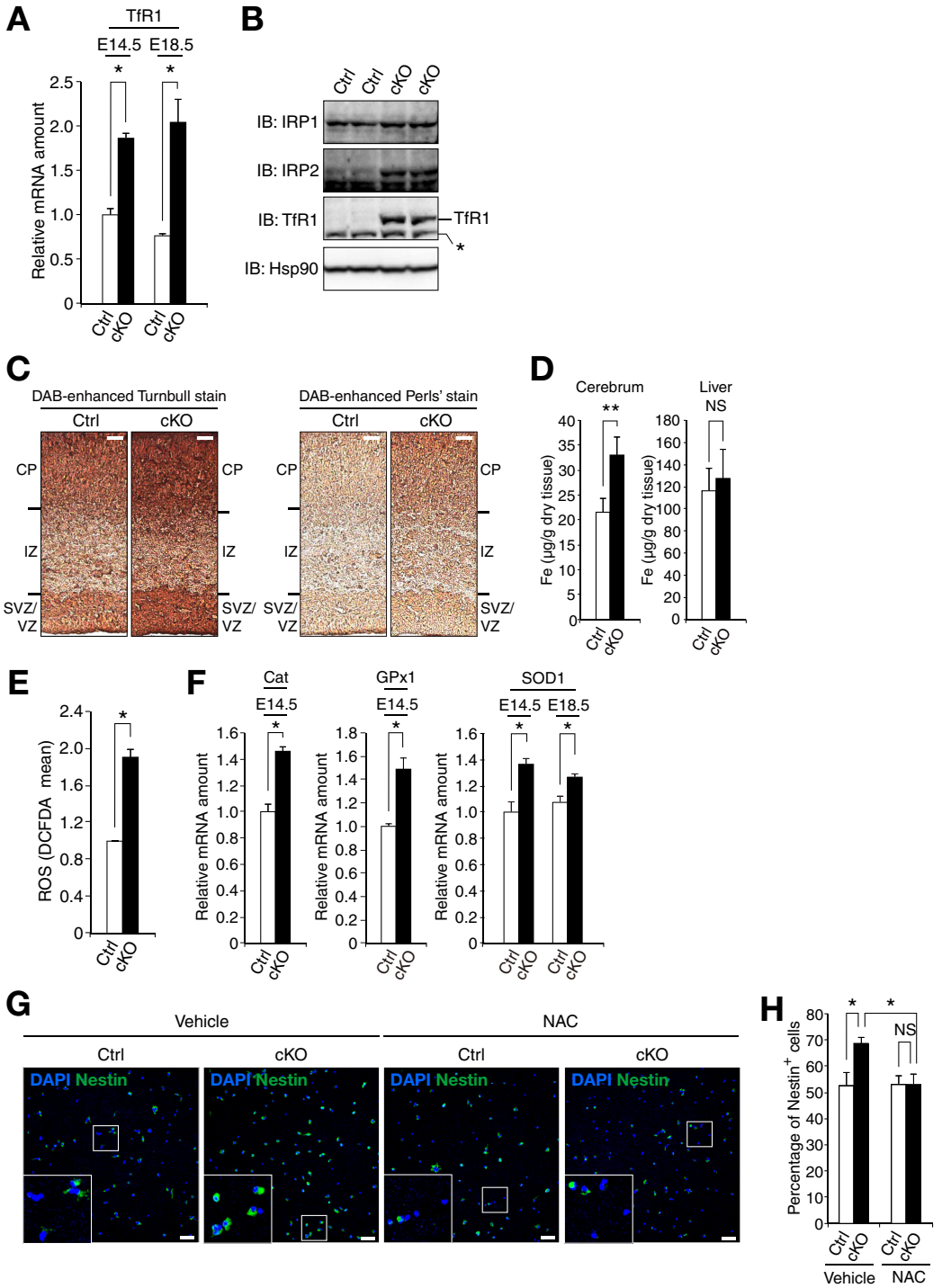

FIG 5 Iron accumulation and oxidative stress in the brain of *Fbxl5* cKO mouse embryos. (A) RT and real-time PCR analysis of TfR1 mRNA in the brain of control and *Fbxl5* cKO mice at E14.5 or E18.5. Normalized data from three independent experiments are expressed relative to the corresponding values for control mice at E14.5. (B) Immunoblot analysis of forebrain extracts from E18.5 mice of the two genotypes with antibodies to the indicated proteins. The asterisk indicates a nonspecific band. (C) DAB-enhanced Turnbull or Perls' staining of the forebrain of E18.5 control and *Fbxl5* cKO mice. (D) Nonheme iron content of the cerebrum and liver of control ($n = 3$) and *Fbxl5* cKO ($n = 3$) mice at E18.5. (E) Flow cytometric analysis of DCFDA fluorescence in neurospheres derived from the E14.5 forebrain of the two genotypes. The ROS level in the neurospheres was assessed by determination of the relative mean fluorescence intensity in three independent experiments. (F) RT and real-time PCR analysis of catalase (Cat), GPx1, and SOD1 mRNAs in the forebrain of E14.5 and E18.5 mice. Data are from three independent experiments. (G) Immunofluorescence analysis of nestin in neurospheres derived from the forebrain of control or *Fbxl5* cKO mice at E14.5. The cells were cultured with 1 mM NAC or vehicle for 3 days under differentiation-inducing conditions. Nuclei were stained with DAPI. The boxed areas are shown at higher magnification in the insets. (H) Quantitative analysis of nestin-positive cells in sections similar to those in shown in panel G. Data are from three independent experiments. Scale bars, 50 μm. All quantitative data are means ± SEM. *, $P < 0.05$; **, $P < 0.01$ (Student's *t* test).

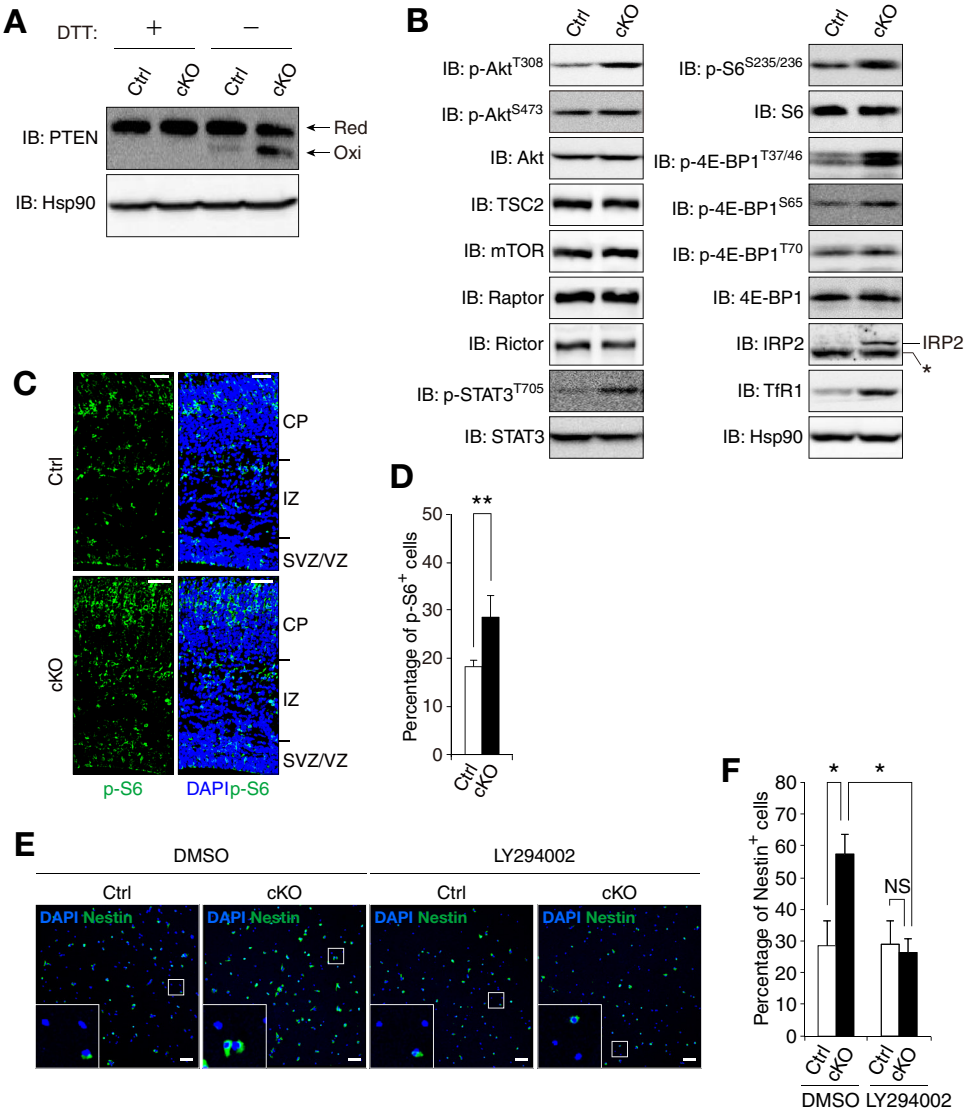

FIG 6 Activation of mTOR signaling in the brain of *Fbxl5* cKO mouse embryos. (A) Immunoblot analysis of PTEN in forebrain extracts from E18.5 control and *Fbxl5* cKO mice. Electrophoresis was performed under reducing [+ dithiothreitol (DTT)] or nonreducing (− DTT) conditions. The positions of reduced (Red) and oxidized (Oxi) forms of PTEN are indicated. (B) Immunoblot analysis of forebrain extracts from E18.5 mice of the two genotypes with antibodies to total or phosphorylated (p-) forms of the indicated proteins. The asterisk indicates a nonspecific band. (C) Immunohistofluorescence staining of phosphorylated S6 in coronal sections of the cortex at E18.5. Nuclei were stained with DAPI. Scale bars, 50 μm. (D) Quantification of cells positive for phospho-S6 in sections ($n = 3$ mice, three sections per mouse) similar to those shown in panel C. Data are means ± SEM. **, $P < 0.01$ (Student's t test). (E) Immunofluorescence analysis of nestin in neurospheres derived from the cerebrum of control or *Fbxl5* cKO mice at E14.5. The cells were cultured with 10 μM LY294002 or DMSO vehicle for 3 days under differentiation-inducing conditions. Nuclei were stained with DAPI. The boxed areas are shown at higher magnification in the insets. Scale bars, 50 μm. (F) Quantitative analysis of cells positive for nestin in experiments similar to the experiment shown in panel E. Data are means ± SEM from three independent experiments. *, $P < 0.05$ (Student's t test).

4E-BP1 in the mutant forebrain was prevented by rapamycin treatment (Fig. 7E). Consistent with these *in vivo* data, the increase in the number of cells positive for phosphorylated S6 or for GFAP apparent in *Fbxl5* cKO neurospheres was attenuated by rapamycin (Fig. 7F to H). Finally, the increased proliferation of nestin-positive NSPCs in neurospheres derived from *Fbxl5* cKO mice was not significant after treatment with rapamycin (Fig. 7I and J). Collectively, these results suggested that the increase in the number of NSPCs in *Fbxl5* cKO mice is attributable to aberrant activation of mTOR signaling.

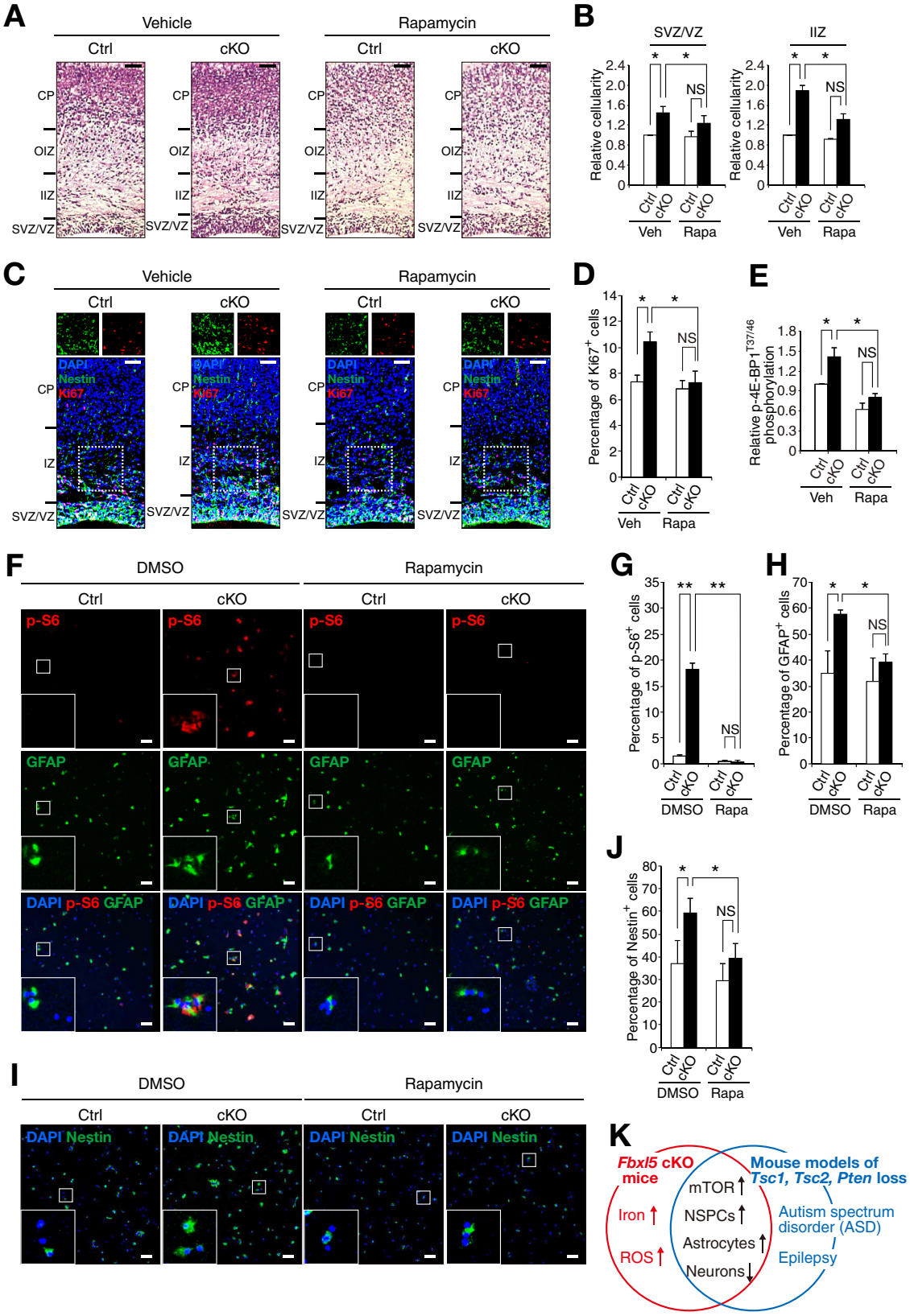

FIG 7 Inhibition of mTOR ameliorates the impaired function of FBXL5-deficient NSPCs. (A) H&E staining of coronal sections of the forebrain of control and *Fbxl5* cKO mouse embryos exposed to rapamycin (Rapa) or vehicle (Veh) from E14.5 to E18.5 before analysis. (B) Quantification of relative cell numbers in the VZ/SVZ and inner IZ regions of sections ($n = 3$ mice, three sections per mouse) similar to those shown in panel A. (C) Immunohistofluorescence staining of nestin and Ki67 in coronal sections of the forebrain for embryos exposed to rapamycin or vehicle as described for panel A. Nuclei were stained with DAPI. (D) Quantification of Ki67$^+$ cells in sections ($n = 3$ mice, three sections per mouse)

(Continued on next page)

DISCUSSION

The present study reveals that FBXL5 is a key regulator of iron levels in embryonic NSPCs and that, as such, it ensures the proper maintenance and differentiation of these cells. Furthermore, we show that FBXL5 regulates NSPC expansion by affecting signaling molecules downstream of ROS and mTOR that have previously been implicated in NSPC proliferation (33, 34).

Whereas some previous studies have suggested that increased ROS levels in NSPCs in the SVZ of the mouse forebrain might be associated with the proliferative or activation status of these cells (33, 35), others based on the conditional deletion of *Foxo* or *Fip200*, both of which contribute to the regulation of intracellular ROS production, have suggested that increased ROS levels in NSPCs result in cell death (36–38). These previous findings have led to the proposal that moderate ROS levels promote both symmetric and asymmetric division of NSPCs, whereas levels that are too high impede NSPC division or eventually result in cell death (30). It is therefore plausible that ROS levels in the brain of *Fbxl5* cKO embryos are within the range of those that promote NSPC proliferation.

An association between mTOR activity and iron concentration has been suggested by both *in vitro* and *in vivo* studies (39). The activity of mTOR was thus found to be reduced by iron chelation in monkey COS-1 cells (40), human myeloid leukemia K562 cells (41), and red blood cells from mice challenged with a low-iron diet (42). On the other hand, the activity of the mTOR-containing complexes mTORC1 and mTORC2 was shown to be increased in the forebrain of two genetic mouse models of iron deficiency (CAMKIIα-Cre/DMT1$^{flox/flox}$ and CAMKIIα-tTA-driven overexpression of a nonfunctional dominant negative form of TfR1) (43). These apparently inconsistent results suggest that the effect of iron deficiency on mTOR activity might be context dependent. In the case of *Fbxl5* cKO mice, we found that increased iron levels result in activation of mTOR signaling *in vivo*, likely through a distinct mechanism, that is, oxidative stress-mediated inactivation of PTEN. Further studies of the effects of iron status in different tissues are warranted to provide further insight into the regulation of mTOR signaling by this element.

Our conditional mouse model recapitulates several distinctive neurodevelopmental phenotypes of PTEN inactivation and mTOR activation, including aberrant expansion of VZ/SVZ regions, increased frequency of astrocytes, and altered cortical neurogenesis (34, 44–46). We found that the level of STAT3 phosphorylation was increased in the FBXL5-deficient brain. STAT3 was previously shown to act in a synergistic manner with mTOR to induce the transcriptional activation of STAT3 target genes, such as those for GFAP and serpinA3 (47). Such a mechanism may explain the link between mTOR hyperactivation and both an increased frequency of astrocytes and neuronal loss in the developing forebrain (34). Given that such features have been suggested to be responsible for early neurodevelopmental conditions such as epilepsy and autism spectrum disorder (45, 48), our results provide a possible connection between excess iron and mTOR activation under these conditions (Fig. 7K). The amount of non-protein-bound iron has recently been shown to be increased in the brain of a rodent model of autism as well as in human patients (17, 49). Whether mTOR signaling is in part responsible for iron overload pathophysiology warrants further investigation with the use of preclinical model systems (18, 20). If so, therapeutic approaches based on both iron chelation and mTOR inhibition may prove effective for human neurological diseases.

FIG 7 Legend (Continued)
similar to those shown in panel C. (E) Quantification of the relative 4E-BP1 phosphorylation level by immunoblot analysis of forebrain extracts from embryos treated with rapamycin or vehicle as described for panel A. (F and I) Immunocytofluorescence staining of phospho-S6 and GFAP or of nestin in neurospheres derived from control or *Fbxl5* cKO embryos and cultured in the presence of 100 nM rapamycin or DMSO vehicle for 3 days under differentiation-inducing conditions. Nuclei were stained with DAPI. (G, H, and J) Quantification of cells positive for phospho-S6, GFAP, or nestin, as indicated, in experiments similar to those shown in panels F and I. Data are from three independent experiments. (K) Molecular and other phenotypes shared by *Fbxl5* cKO mice and mouse models of mTOR activation in the developing brain. See the text for details. The boxed areas in panels C, F, and I are shown at higher magnification in the insets. Scale bars, 50 μm. All quantitative data are means ± SEM. *, $P < 0.05$; **, $P < 0.01$ (Student's *t* test).

MATERIALS AND METHODS

Mice. *Fbxl5*$^{flox/flox}$ mice (10) were intercrossed with *Nestin-Cre* transgenic mice (50) to produce *Nestin-Cre/Fbxl5*$^{flox/flox}$ offspring. Mice were genotyped by PCR analysis of genomic DNA with primers for *Fbxl5* (5′-CAGGCAAGTGGACAGAAAAGCAAC-3′, 5′-CATTTAGCCCAGTACCTGCCTGTG-3′, and 5′-TGTCAAA GACAAAACCAGAGTCGG-3′) and for *Nestin-Cre* (5′-TCGACCAGTTTAGTTACCC-3′ and 5′-AGGTTCGTTCAC TCATGGA-3′). All animals were maintained under specific-pathogen-free conditions, and all experiments were approved by the animal ethics committee of Kyushu University.

Neurosphere formation and differentiation assays. A neurosphere formation assay was performed as previously described (50). Cortical cells isolated from embryos at embryonic day 14.5 (E14.5) were suspended in Neurobasal medium (Invitrogen) supplemented with 1% penicillin-streptomycin (Invitrogen), 1% L-glutamine (Invitrogen), B27 (Invitrogen), basic fibroblast growth factor (FGF) (20 ng/ml; R&D Systems), and epidermal growth factor (20 ng/ml; Invitrogen) and were then plated at clonal density (2.0×10^4 cells/ml) in Ultra-Low Attachment 24-well plates (Corning) and cultured for 3 to 7 days. For a differentiation assay, dissociated neurospheres (1×10^5 cells) were suspended in Neurobasal medium supplemented with 1% penicillin-streptomycin, 1% L-glutamine, B27, and 1% fetal bovine serum (Gibco), plated on glass coverslips that had been coated with poly-L-lysine (Sigma-Aldrich), placed in 24-well plates, and then cultured for an additional 3 to 7 days. Culture was performed in the absence or presence of *N*-acetylcysteine (NAC; Sigma-Aldrich), LY294002 (Cell Signaling Technology), or rapamycin (R-5000; LC Laboratories).

Immunocytofluorescence analysis. Cells from neurosphere differentiation cultures were fixed for 10 min with 4% paraformaldehyde in phosphate-buffered saline (PBS), permeabilized with 0.1% saponin, and exposed to 5% bovine serum albumin (BSA) before incubation with primary antibodies and Alexa Fluor-conjugated secondary antibodies as described below for tissue sections. The primary antibodies included those to nestin (rat-401; Millipore), to MAP2 (ab7756; Abcam), to GFAP (ZO334; Dako), to O4 (MAB1326; R&D Systems), and to phosphorylated S6 (2211; Cell Signaling Technology).

Iron histochemistry. Pregnant mice were anesthetized by intravenous injection of pentobarbital sodium (648 mg/kg of body weight) and then perfused first with 50 mM hydrogen sulfide in deionized water and then with 4% paraformaldehyde in PBS. Iron was detected in cryostat sections of embryos by diaminobenzidine (DAB)-enhanced Perls' or Turnbull staining. Tissue sections were washed with deionized water, incubated for 30 min with Perls' reagent (5% potassium ferrocyanide in 5% HCl) or Turnbull reagent (5% potassium ferricyanide in 5% HCl), and then washed again in deionized water before incubation at room temperature first for 15 min with unactivated DAB (0.05% DAB in deionized water) and then for 10 min with activated DAB (0.05% DAB in 1% H_2O_2). Tissue sections from control and mutant mice were processed at the same time to allow monitoring and detection of nonspecific staining.

Immunohistofluorescence staining. Immunofluorescence staining of paraffin-embedded or frozen sections was performed as described previously (50). The brain isolated from embryos at E14.5 to E18.5 was fixed overnight at 4°C with 4% paraformaldehyde in PBS. Paraffin-embedded sections (4 μm) were prepared and stained with hematoxylin-eosin (H&E) for routine histological examination or left unstained for immunofluorescence analysis. H&E-stained sections were examined with a light microscope (AxioImager A1; Zeiss), and images were acquired with a digital camera (AxioCam HRc; Zeiss) and AxioVision software (version 4.4; Zeiss). For immunofluorescence analysis, sections were depleted of paraffin, rehydrated, treated for antigen retrieval, and exposed to 5% BSA before incubation overnight at 4°C with primary antibodies. Frozen sections (16 μm) were also exposed to 5% BSA before incubation overnight at 4°C with primary antibodies. The primary antibodies included those to pHH3 (9701; Cell Signaling Technology), to Ki67 (SP6; Thermo Scientific), to cleaved caspase-3 (9661; Cell Signaling Technology), to Pax6 (AB5409; Chemicon), to nestin (rat-401; Millipore), to Tbr1 (ab31940; Abcam), to Tbr2 (AB2283; Millipore), to Cux1 (sc-13024; Santa Cruz Biotechnology), to MAP2 (ab7756; Abcam), to GFAP (ZO334; Dako), to NG2 (AB5320; Millipore), to myelin basic protein (MBP) (AB980; Millipore), to phospho-S6 (2211; Cell Signaling Technology), and to ferritin (F6136; Sigma-Aldrich). Sections were counterstained with 4′,6-diamidino-2-phenylindole (DAPI). Immune complexes were detected with secondary antibodies labeled with Alexa Fluor 488 or 546 (Invitrogen). Images were acquired with a laser scanning confocal microscope (LSM700; Zeiss) and ZEN imaging software (Zeiss).

BrdU labeling. Pulse-labeling with bromodeoxyuridine (BrdU; Sigma-Aldrich) was performed by intraperitoneal injection of pregnant dams at E18.5 with BrdU (50 μg/g) 1 h before isolation of embryos for analysis. The embryos were fixed in PBS containing 4% paraformaldehyde and embedded in paraffin. Sections were stained overnight at 4°C with biotin-conjugated mouse antibodies to BrdU (BD Biosciences), and immune complexes were then detected with Alexa Fluor 488-conjugated streptavidin (Invitrogen). For analysis of cells that had recently exited from the cell cycle, pregnant dams were injected with BrdU at E14.5, and embryos were isolated 24 h later for immunostaining with antibodies to BrdU and with those to Ki67 (SP6; Thermo Scientific). The percentage of cells labeled with BrdU that were negative for Ki67 was determined.

Rapamycin administration. Rapamycin (R-5000; LC Laboratories) was prepared as a stock solution (10 mg/ml) in dimethyl sulfoxide (DMSO), which was stored at −20°C and then diluted before each administration with a solution containing 5% Tween 80 and 5% polyethylene glycol 400 (Sigma). Pregnant dams were injected intraperitoneally with rapamycin (0.2 mg/kg) or vehicle at E14.5, and embryos were isolated for analysis at E18.5.

Total nonheme iron determination. Total nonheme iron was measured as described previously (10, 51). Tissue was dried for 48 h at 45°C, weighed, digested for 48 h at 65°C in acid solution (10% trichloroacetic acid in 10% HCl), and then mixed with 5 volumes of chromogen solution (0.01% bathophenanthroline-disulfonic acid, 0.1% thioglycolic acid, 7 M sodium acetate) and incubated for 10

min at room temperature before measurement of absorbance at 535 nm. A certified iron standard solution (Nakarai) was used to determine iron levels.

Intracellular ROS measurement. Dissociated neurospheres derived from E14.5 mouse cortical tissue were labeled for 30 min at room temperature with 5 μM 2′,7′-dichlorofluorescein diacetate (DCFDA; Invitrogen) in PBS, washed three times with PBS, suspended in Neurobasal medium containing propidium iodide (5 μg/ml), and incubated for 1 h at room temperature before flow cytometric analysis with a FACSCalibur instrument (BD Biosciences) and Cell Quest software (BD Biosciences).

RT and real-time PCR analysis. Reverse transcription (RT) and real-time PCR analysis were performed as previously described (52) with mRNA isolated from embryos with the use of the Isogen reagent (Nippon Gene). The sequences of PCR primers (forward and reverse, respectively) were 5′-TCTTCCTCCTGAGGTAATGCTGTCC-3′ and 5′-CACAAAGATCCTGTTTTTGCCAGC-3′ for FBXL5, 5′-GGTGATCCATACACACCTGGCTT-3′ and 5′-TGATGACTGAGATGGCGGAA-3′ for TfR1, 5′-GCAGATACCTGTGAACTGTC-3′ and 5′-GTAGAATGTCCGCACCTGAG-3′ for catalase, 5′-CCTCAAGTACGTCCGACCTG-3′ and 5′-CAATGTCGTTGCGGCACACC-3′ for GPx1, 5′-AAGGCCGTGTGCGTGCTGAA-3′ and 5′-CAGGTCTCCAACATGCCTCT-3′ for SOD1, and 5′-GCTTCCTGGAGGGTGTCC-3′ and 5′-GGACTCGTTTGTACCCGTTG-3′ for RPLP0 (ribosomal protein, large, P0). Data were normalized by the corresponding amount of RPLP0 mRNA.

Immunoblot analysis. Immunoblot analysis was performed as previously described (53) with antibodies to IRP1 (sc-14216; Santa Cruz Biotechnology), to IRP2 (generated by K. Iwai, Osaka University), to TfR1 (13-6800; Invitrogen), to ferritin (F6136; Sigma-Aldrich), to Akt (2967), to Thr^{308}-phosphorylated Akt (2965), to Ser^{473}-phosphorylated Akt (4060), to TSC2 (4308), to mTOR (2983), to Raptor (2280), to Rictor (2114), to S6 (2217), to Ser$^{235/236}$-phosphorylated S6 (2211), to 4E-BP1 (9644), to 4E-BP1 phosphorylated at Thr$^{37/46}$ (2855), Ser^{65} (9451), or Thr^{70} (9455), to STAT3 (9132), to Tyr^{705}-phosphorylated STAT3 (9131), and to Hsp90 (610419; BD Biosciences). Identification of reduced and oxidized forms of PTEN was performed as described previously (54) with antibodies to PTEN (9188). All antibodies were from Cell Signaling Technology unless indicated otherwise. The band intensities were normalized with corresponding Hsp90 abundance and quantitated with the use of ImageJ software (National Institutes of Health).

Statistical analysis. Results for continuous variables are presented as means ± standard errors of the means (SEM). Comparisons between two groups were performed with Student's *t* test for independent samples. A *P* value of <0.05 was considered statistically significant.

ACKNOWLEDGMENTS

We thank E. Koba, K. Motomura, and N. Kinoshita for technical assistance.

We declare that we have no conflicts of interest.

This study was performed as a research program of the Project for Development of Innovative Research on Cancer Therapeutics (P-Direct) of the Ministry of Education, Culture, Sports, Science, and Technology (MEXT) of Japan. It was also funded in part by KAKENHI grants (25221303 and 26640080) from MEXT. T.Y. was supported by a Research Fellowship of the Japan Society for the Promotion of Science for Young Scientists.

REFERENCES

1. Rouault TA, Tong WH. 2005. Iron-sulphur cluster biogenesis and mitochondrial iron homeostasis. Nat Rev Mol Cell Biol 6:345–351. https://doi.org/10.1038/nrm1620.
2. Hentze MW, Muckenthaler MU, Galy B, Camaschella C. 2010. Two to tango: regulation of mammalian iron metabolism. Cell 142:24–38. https://doi.org/10.1016/j.cell.2010.06.028.
3. De Domenico I, McVey Ward D, Kaplan J. 2008. Regulation of iron acquisition and storage: consequences for iron-linked disorders. Nat Rev Mol Cell Biol 9:72–81. https://doi.org/10.1038/nrm2295.
4. Torti SV, Torti FM. 2011. Ironing out cancer. Cancer Res 71:1511–1514. https://doi.org/10.1158/0008-5472.CAN-10-3614.
5. Weinberg ED. 2010. The hazards of iron loading. Metallomics 2:732–740. https://doi.org/10.1039/c0mt00023j.
6. Nakayama KI, Nakayama K. 2006. Ubiquitin ligases: cell-cycle control and cancer. Nat Rev Cancer 6:369–381. https://doi.org/10.1038/nrc1881.
7. Wang Z, Liu P, Inuzuka H, Wei W. 2014. Roles of F-box proteins in cancer. Nat Rev Cancer 14:233–247. https://doi.org/10.1038/nrc3700.
8. Salahudeen AA, Thompson JW, Ruiz JC, Ma HW, Kinch LN, Li Q, Grishin NV, Bruick RK. 2009. An E3 ligase possessing an iron-responsive hemerythrin domain is a regulator of iron homeostasis. Science 326:722–726. https://doi.org/10.1126/science.1176326.
9. Vashisht AA, Zumbrennen KB, Huang X, Powers DN, Durazo A, Sun D, Bhaskaran N, Persson A, Uhlen M, Sangfelt O, Spruck C, Leibold EA, Wohlschlegel JA. 2009. Control of iron homeostasis by an iron-regulated ubiquitin ligase. Science 326:718–721. https://doi.org/10.1126/science.1176333.
10. Moroishi T, Nishiyama M, Takeda Y, Iwai K, Nakayama KI. 2011. The FBXL5-IRP2 axis is integral to control of iron metabolism in vivo. Cell Metab 14:339–351. https://doi.org/10.1016/j.cmet.2011.07.011.
11. Ruiz JC, Bruick RK. 2014. F-box and leucine-rich repeat protein 5 (FBXL5): sensing intracellular iron and oxygen. J Inorg Biochem 133:73–77. https://doi.org/10.1016/j.jinorgbio.2014.01.015.
12. Fietz SA, Huttner WB. 2011. Cortical progenitor expansion, self-renewal and neurogenesis-a polarized perspective. Curr Opin Neurobiol 21:23–35. https://doi.org/10.1016/j.conb.2010.10.002.
13. Kriegstein A, Alvarez-Buylla A. 2009. The glial nature of embryonic and adult neural stem cells. Annu Rev Neurosci 32:149–184. https://doi.org/10.1146/annurev.neuro.051508.135600.
14. Kalani MY, Cheshier SH, Cord BJ, Bababeygy SR, Vogel H, Weissman IL, Palmer TD, Nusse R. 2008. Wnt-mediated self-renewal of neural stem/progenitor cells. Proc Natl Acad Sci U S A 105:16970–16975. https://doi.org/10.1073/pnas.0808616105.
15. Belanger M, Allaman I, Magistretti PJ. 2011. Brain energy metabolism: focus on astrocyte-neuron metabolic cooperation. Cell Metab 14:724–738. https://doi.org/10.1016/j.cmet.2011.08.016.
16. Knobloch M, Braun SM, Zurkirchen L, von Schoultz C, Zamboni N, Arauzo-Bravo MJ, Kovacs WJ, Karalay O, Suter U, Machado RA, Roccio M, Lutolf MP, Semenkovich CF, Jessberger S. 2013. Metabolic control of adult neural stem cell activity by Fasn-dependent lipogenesis. Nature 493:226–230. https://doi.org/10.1038/nature11689.
17. De Felice C, Della Ragione F, Signorini C, Leoncini S, Pecorelli A, Ciccoli L, Scalabri F, Marracino F, Madonna M, Belmonte G, Ricceri L, De Filippis B, Laviola G, Valacchi G, Durand T, Galano JM, Oger C, Guy A, Bultel-Ponce V, Guy J, Filosa S, Hayek J, D'Esposito M. 2014. Oxidative brain

damage in Mecp2-mutant murine models of Rett syndrome. Neurobiol Dis 68:66–77. https://doi.org/10.1016/j.nbd.2014.04.006.
18. Rouault TA. 2013. Iron metabolism in the CNS: implications for neurodegenerative diseases. Nat Rev Neurosci 14:551–564. https://doi.org/10.1038/nrn3453.
19. Weinreb O, Mandel S, Youdim MB, Amit T. 2013. Targeting dysregulation of brain iron homeostasis in Parkinson's disease by iron chelators. Free Radic Biol Med 62:52–64. https://doi.org/10.1016/j.freeradbiomed.2013.01.017.
20. Lei P, Ayton S, Finkelstein DI, Spoerri L, Ciccotosto GD, Wright DK, Wong BX, Adlard PA, Cherny RA, Lam LQ, Roberts BR, Volitakis I, Egan GF, McLean CA, Cappai R, Duce JA, Bush AI. 2012. Tau deficiency induces parkinsonism with dementia by impairing APP-mediated iron export. Nat Med 18:291–295. https://doi.org/10.1038/nm.2613.
21. Raven EP, Lu PH, Tishler TA, Heydari P, Bartzokis G. 2013. Increased iron levels and decreased tissue integrity in hippocampus of Alzheimer's disease detected in vivo with magnetic resonance imaging. J Alzheimers Dis 37:127–136. https://doi.org/10.3233/JAD-130209.
22. Xiong P, Chen X, Guo C, Zhang N, Ma B. 2012. Baicalin and deferoxamine alleviate iron accumulation in different brain regions of Parkinson's disease rats. Neural Regen Res 7:2092–2098. https://doi.org/10.3969/j.issn.1673-5374.2012.27.002.
23. Regensburger M, Prots I, Winner B. 2014. Adult hippocampal neurogenesis in Parkinson's disease: impact on neuronal survival and plasticity. Neural Plast 2014:454696. https://doi.org/10.1155/2014/454696.
24. van den Berge SA, van Strien ME, Hol EM. 2013. Resident adult neural stem cells in Parkinson's disease—the brain's own repair system? Eur J Pharmacol 719:117–127. https://doi.org/10.1016/j.ejphar.2013.04.058.
25. Turgeon B, Meloche S. 2009. Interpreting neonatal lethal phenotypes in mouse mutants: insights into gene function and human diseases. Physiol Rev 89:1–26. https://doi.org/10.1152/physrev.00040.2007.
26. Dehay C, Kennedy H. 2007. Cell-cycle control and cortical development. Nat Rev Neurosci 8:438–450. https://doi.org/10.1038/nrn2097.
27. Arnold SJ, Huang GJ, Cheung AF, Era T, Nishikawa S, Bikoff EK, Molnar Z, Robertson EJ, Groszer M. 2008. The T-box transcription factor Eomes/Tbr2 regulates neurogenesis in the cortical subventricular zone. Genes Dev 22:2479–2484. https://doi.org/10.1101/gad.475408.
28. Sessa A, Mao CA, Hadjantonakis AK, Klein WH, Broccoli V. 2008. Tbr2 directs conversion of radial glia into basal precursors and guides neuronal amplification by indirect neurogenesis in the developing neocortex. Neuron 60:56–69. https://doi.org/10.1016/j.neuron.2008.09.028.
29. Meguro R, Asano Y, Iwatsuki H, Shoumura K. 2003. Perfusion-Perls and -Turnbull methods supplemented by DAB intensification for nonheme iron histochemistry: demonstration of the superior sensitivity of the methods in the liver, spleen, and stomach of the rat. Histochem Cell Biol 120:73–82. https://doi.org/10.1007/s00418-003-0539-y.
30. Schieber M, Chandel NS. 2014. ROS function in redox signaling and oxidative stress. Curr Biol 24:R453–R462. https://doi.org/10.1016/j.cub.2014.03.034.
31. Kwon J, Lee SR, Yang KS, Ahn Y, Kim YJ, Stadtman ER, Rhee SG. 2004. Reversible oxidation and inactivation of the tumor suppressor PTEN in cells stimulated with peptide growth factors. Proc Natl Acad Sci U S A 101:16419–16424. https://doi.org/10.1073/pnas.0407396101.
32. Leslie NR. 2006. The redox regulation of PI 3-kinase-dependent signaling. Antioxid Redox Signal 8:1765–1774. https://doi.org/10.1089/ars.2006.8.1765.
33. Le Belle JE, Orozco NM, Paucar AA, Saxe JP, Mottahedeh J, Pyle AD, Wu H, Kornblum HI. 2011. Proliferative neural stem cells have high endogenous ROS levels that regulate self-renewal and neurogenesis in a PI3K/Akt-dependent manner. Cell Stem Cell 8:59–71. https://doi.org/10.1016/j.stem.2010.11.028.
34. Magri L, Cambiaghi M, Cominelli M, Alfaro-Cervello C, Cursi M, Pala M, Bulfone A, Garcia-Verdugo JM, Leocani L, Minicucci F, Poliani PL, Galli R. 2011. Sustained activation of mTOR pathway in embryonic neural stem cells leads to development of tuberous sclerosis complex-associated lesions. Cell Stem Cell 9:447–462. https://doi.org/10.1016/j.stem.2011.09.008.
35. Kennedy KA, Sandiford SD, Skerjanc IS, Li SS. 2012. Reactive oxygen species and the neuronal fate. Cell Mol Life Sci 69:215–221. https://doi.org/10.1007/s00018-011-0807-2.
36. Paik JH, Ding Z, Narurkar R, Ramkissoon S, Muller F, Kamoun WS, Chae SS, Zheng H, Ying H, Mahoney J, Hiller D, Jiang S, Protopopov A, Wong WH, Chin L, Ligon KL, DePinho RA. 2009. FoxOs cooperatively regulate diverse pathways governing neural stem cell homeostasis. Cell Stem Cell 5:540–553. https://doi.org/10.1016/j.stem.2009.09.013.
37. Chuikov S, Levi BP, Smith ML, Morrison SJ. 2010. Prdm16 promotes stem cell maintenance in multiple tissues, partly by regulating oxidative stress. Nat Cell Biol 12:999–1006. https://doi.org/10.1038/ncb2101.
38. Wang CR, Liang CC, Bian ZC, Zhu Y, Guan JL. 2013. FIP200 is required for maintenance and differentiation of postnatal neural stem cells. Nat Neurosci 16:532–542. https://doi.org/10.1038/nn.3365.
39. Guan P, Wang N. 2014. Mammalian target of rapamycin coordinates iron metabolism with iron-sulfur cluster assembly enzyme and tristetraprolin. Nutrition 30:968–974. https://doi.org/10.1016/j.nut.2013.12.016.
40. Ndong M, Kazami M, Suzuki T, Uehara M, Katsumata S, Inoue H, Kobayashi K, Tadokoro T, Suzuki K, Yamamoto Y. 2009. Iron deficiency down-regulates the Akt/TSC1-TSC2/mammalian target of rapamycin signaling pathway in rats and in COS-1 cells. Nutr Res 29:640–647. https://doi.org/10.1016/j.nutres.2009.09.007.
41. Ohyashiki JH, Kobayashi C, Hamamura R, Okabe S, Tauchi T, Ohyashiki K. 2009. The oral iron chelator deferasirox represses signaling through the mTOR in myeloid leukemia cells by enhancing expression of REDD1. Cancer Sci 100:970–977. https://doi.org/10.1111/j.1349-7006.2009.01131.x.
42. Knight ZA, Schmidt SF, Birsoy K, Tan K, Friedman JM. 2014. A critical role for mTORC1 in erythropoiesis and anemia. eLife 3:e01913. https://doi.org/10.7554/eLife.01913.
43. Fretham SJ, Carlson ES, Georgieff MK. 2013. Neuronal-specific iron deficiency dysregulates mammalian target of rapamycin signaling during hippocampal development in nonanemic genetic mouse models. J Nutr 143:260–266. https://doi.org/10.3945/jn.112.168617.
44. Gregorian C, Nakashima J, Le Belle J, Ohab J, Kim R, Liu A, Smith KB, Groszer M, Garcia AD, Sofroniew MV, Carmichael ST, Kornblum HI, Liu X, Wu H. 2009. Pten deletion in adult neural stem/progenitor cells enhances constitutive neurogenesis. J Neurosci 29:1874–1886. https://doi.org/10.1523/JNEUROSCI.3095-08.2009.
45. Zeng LH, Rensing NR, Zhang B, Gutmann DH, Gambello MJ, Wong M. 2011. Tsc2 gene inactivation causes a more severe epilepsy phenotype than Tsc1 inactivation in a mouse model of tuberous sclerosis complex. Hum Mol Genet 20:445–454. https://doi.org/10.1093/hmg/ddq491.
46. Amiri A, Cho W, Zhou J, Birnbaum SG, Sinton CM, McKay RM, Parada LF. 2012. Pten deletion in adult hippocampal neural stem/progenitor cells causes cellular abnormalities and alters neurogenesis. J Neurosci 32:5880–5890. https://doi.org/10.1523/JNEUROSCI.5462-11.2012.
47. Yokogami K, Wakisaka S, Avruch J, Reeves SA. 2000. Serine phosphorylation and maximal activation of STAT3 during CNTF signaling is mediated by the rapamycin target mTOR. Curr Biol 10:47–50. https://doi.org/10.1016/S0960-9822(99)00268-7.
48. Costa-Mattioli M, Monteggia LM. 2013. mTOR complexes in neurodevelopmental and neuropsychiatric disorders. Nat Neurosci 16:1537–1543. https://doi.org/10.1038/nn.3546.
49. Pecorelli A, Leoncini S, De Felice C, Signorini C, Cerrone C, Valacchi G, Ciccoli L, Hayek J. 2013. Non-protein-bound iron and 4-hydroxynonenal protein adducts in classic autism. Brain Dev 35:146–154. https://doi.org/10.1016/j.braindev.2012.03.011.
50. Matsumoto A, Onoyama I, Sunabori T, Kageyama R, Okano H, Nakayama KI. 2011. Fbxw7-dependent degradation of Notch is required for control of "stemness" and neuronal-glial differentiation in neural stem cells. J Biol Chem 286:13754–13764. https://doi.org/10.1074/jbc.M110.194936.
51. Patel BN, Dunn RJ, Jeong SY, Zhu QZ, Julien JP, David S. 2002. Ceruloplasmin regulates iron levels in the CNS and prevents free radical injury. J Neurosci 22:6578–6586.
52. Moroishi T, Yamauchi T, Nishiyama M, Nakayama KI. 2014. HERC2 targets the iron regulator FBXL5 for degradation and modulates iron metabolism. J Biol Chem 289:16430–16441. https://doi.org/10.1074/jbc.M113.541490.
53. Yamauchi T, Nishiyama M, Moroishi T, Yumimoto K, Nakayama KI. 2014. MDM2 mediates nonproteolytic polyubiquitylation of the DEAD-box RNA helicase DDX24. Mol Cell Biol 34:3321–3340. https://doi.org/10.1128/MCB.00320-14.
54. Lee SR, Yang KS, Kwon J, Lee C, Jeong W, Rhee SG. 2002. Reversible inactivation of the tumor suppressor PTEN by H_2O_2. J Biol Chem 277:20336–20342. https://doi.org/10.1074/jbc.M111899200.